RSC Advances

PAPER

View Article Online
View Journal | View Issue

Cite this: *RSC Adv.*, 2020, **10**, 39037

Nanostructured copper molybdates as promising bifunctional electrocatalysts for overall water splitting and CO_2 reduction†

Atefeh Rahmani[a] and Hossein Farsi *[ab]

Received 10th September 2020
Accepted 20th October 2020

DOI: 10.1039/d0ra07783f

rsc.li/rsc-advances

Overall water splitting and CO_2 reduction are two very important reactions from the environmental viewpoint. The former produces hydrogen as a clean fuel and the latter decreases the amount of CO_2 emissions and thus reduces greenhouse effects. Here, we prepare two types of copper molybdate, $CuMoO_4$ and $Cu_3Mo_2O_9$, and electrochemically investigate them for water splitting and CO_2 reduction. Our findings show that $Cu_3Mo_2O_9$ is a better electrocatalyst for full water splitting compared to $CuMoO_4$. It provides overpotentials, which are smaller than the overpotentials of $CuMoO_4$ by around 0.14 V at a current density of 1 mA cm^{-2} and 0.10 V at −0.4 mA cm^{-2}, for water oxidation and hydrogen evolution reactions, respectively. However, $CuMoO_4$ adsorbs CO_2 and the reduced intermediates/products more strongly than $Cu_3Mo_2O_9$. Such different behaviors of these electrocatalysts can be attributed to their different unit cells.

1. Introduction

Fossil fuels are diminishing resources that contribute notably to environmental pollution, so developing sustainable energy sources suitable for our growing energy requirements is critical for the survival of humankind.[1,2] An abiotic component of promising renewable energy infrastructure with no reliance on fossil fuels and no carbon dioxide emission is the splitting of water into hydrogen and oxygen.[3,4] In photoelectrochemical (PEC) water splitting, solar energy is directly converted to fuel by light-absorbing semiconductors. As a new generation energy carrier, solar hydrogen will play an important role in our lives because it is storable, transportable, and convertible into efficient electricity in fuel cells, as well as being a viable and clean source of power due to its extraordinarily high energy density.[5] During water splitting, the reductive half-reaction with a two-electron transfer mechanism is relatively easier than the oxidative half-reaction involving a four-electron transfer mechanism,[6] which is the most energy-intensive step in the overall water splitting process. Therefore, the slow kinetics of the oxygen evolution reaction, OER, requires a substantial overpotential to generate measurable current densities.[7] A large positive change in Gibbs free energy ($\Delta G^0 = 237.13$ kJ mol^{-1}) causes the full water splitting reaction to be thermodynamically an uphill reaction.[8] From this perspective, it is challenging to design highly effective photocatalysts while considering crucial parameters in the development of suitable semiconductors. These parameters include band gap width, optical absorption edge, stability against photocorrosion/lifetime, solar photons to current efficiency, cost-effectiveness, catalytic activity and surface structure.[9–11] Furthermore, a high degree of crystallinity, *i.e.* a smaller amount of defects, is often required for water splitting because recombination between photogenerated carriers is particularly a serious problem in uphill reactions. Beginning with the discovery of Fujishima and Honda in the early 1970s, metal oxide or mixed-metal oxide semiconductors have been well studied as water splitting photoanodes due to their low cost and high stability in aqueous environments.[12] Because the mixture of two metals in an oxide matrix can generate materials with unique chemical and physical properties, much consideration has been paid to the mixed-metal oxides, such as metal titanates, metal tungstates and metal molybdates.

Moreover, the growing CO_2 emission is an inevitable result of fossil fuels consumption because of the accessibility, diversity and high energy density of these fuels. However, the ever-increasing use of fossil fuels will cause dependence on them despite their limited reserves; additionally, global warming, drastic environmental changes and an intense threat to human survival are other issues associated with the use of fossil fuels. To resolve these issues, the best approach is to convert CO_2 into carbon-containing fuels as a renewable energy resource.[13,14] Recently, electrochemical reduction of accumulative CO_2 has been considered as a feasible strategy for the conversion and utilization of this gas. This process was reported for the first

[a]*Department of Chemistry, University of Birjand, Birjand, Iran. E-mail: hofarsi@birjand.ac.ir*

[b]*Developing Nanomaterials for Environmental Protection Research Lab, University of Birjand, Birjand, Iran*

† Electronic supplementary information (ESI) available. See DOI: 10.1039/d0ra07783f

time by Sir B. C. Brodie in 1873 and later in the 1990s by Hori *et al.*[15,16] However, many efforts have been carried out to overcome usual challenges, such as poor efficiency because of kinetic barrier for stable molecules, weak selectivity resulting from reduction products competition, side reactions and hydrogen evolution reaction (HER).[17,18] Therefore, probing new electrocatalysts that efficiently reduce CO_2 into liquid fuels, especially in mild conditions, is extremely significant. For this purpose, copper (Cu) and Cu-based electrodes have been investigated as electrocatalyst candidates due to their intrinsic catalytic activity and variation of reduction products, which considerably depend on surface properties and morphology.[19–30] Despite many experimental efforts and computational calculations, the mechanism of CO_2 reduction on Cu electrodes is intricate and the exact reaction path is controversial.[31,32]

With regard to the above studies, it seems that Cu-based mixed oxides can be considered as bifunctional-electrocatalysts, which can electrochemically oxidize water and reduce CO_2. For example, some of the widely studied copper-based photocatalysts for water splitting have been crystalline copper phosphide nanosheet,[33] cuprous oxide composites,[34–36] copper(II) tungstate[37–39] and copper(II) borate.[40] More recently, scientists have tried to find nanomaterials that exhibit remarkable properties to catalyze both hydrogen production and water oxidation reactions when the applied potentials fluctuate between oxidative and reductive conditions in the same reaction electrolyte.[41] A copper-based catalyst composite film was found to be an interesting electrocatalyst for both HER and OER in the same electrolyte.[42]

To the best of our knowledge, there is no report on the application of copper molybdates for these properties. However, over the past several years, different preparations and structures of transition metal molybdates have been widely reported; these include doped,[43,44] layered,[45–47] nanosheet,[48,49] powder,[50] flower-like,[51] nanoplate[52] and micropompons[53] structures. These structures are widely used in the areas of catalysis, magnetic application and energy storage. Furthermore, $CuMoO_4$ is a thermochromic, trisochromic and piezochromic material, so it can be used in pressure and/or temperature sensors. Recently, extensive studies have been conducted on using transition metal molybdates in catalysis/photocatalysis,[43,44,49,53–55] magnetic applications[46,56–58] and lithium batteries;[52] for example, preparation of hybrid $Cu_2O/CuMoO_4$ nanosheet electrodes for high-performance asymmetric supercapacitors,[48] $Cu_3Mo_2O_9$ nanoplates with excellent lithium storage performance[52] and $Cu_3Mo_2O_9$ micropompons with excellent performance in photocatalytic degradation of Congo red under visible light, photocurrent response and lithium storage.[53] Two different compounds of copper molybdate exist with two different chemical formulae of $CuMoO_4$ and $Cu_3Mo_2O_9$. Both of them contain MoO_4 tetrahedra, CuO_6 octahedra and CuO_5 pyramid units. In $CuMoO_4$, six copper–oxygen polyhedra share edges to form a spiral-shaped chain fragment, interconnected by MoO_4 tetrahedra,[59] whereas sharing the edge oxygen atoms of Cu-based polyhedra makes a zigzag ribbon.[60]

The crystal structures of both compounds are shown in Fig. 1; these structures were reproduced by Mercury software[61–63] from the Cambridge Crystallographic Data Center, using their CIF files. Recently, we reported that tungstate-derived copper has a good activity for electrochemical reduction of CO_2,[64] so it is expected here that we have molybdate-derived copper from two different sources, $CuMoO_4$ and $Cu_3Mo_2O_9$, with two different distribution of copper atoms and consequently different activities.

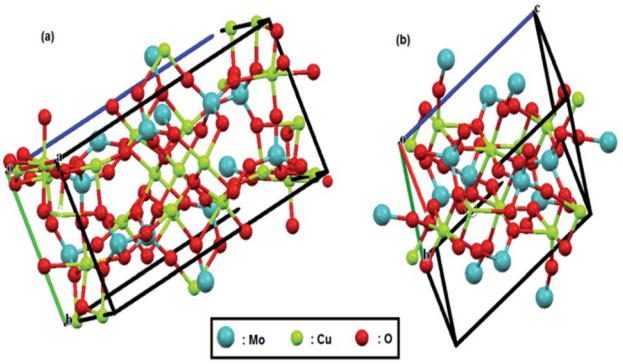

Fig. 1 Crystal structure of (a) $Cu_3Mo_2O_9$ and (b) $CuMoO_4$. Red, green and pale blue balls represent oxygen, copper and molybdenum atoms, respectively.

Due to these different crystal structures, their comparative study as bifunctional catalysts for electrochemical water splitting and CO_2 reduction seems very interesting. In this study, we successfully prepare, characterize and electrochemically investigate both nano-$CuMoO_4$ and nano-$Cu_3Mo_2O_9$ structures.

2. Experimental

2.1. Materials preparation

The reactions were carried out under air at room pressure. High purity (>99%) AR grade copper nitrate $Cu(NO_3)_2 \cdot 3H_2O$, sodium molybdate $Na_2MoO_4 \cdot 2H_2O$, citric acid and ammonium heptamolybdate, $(NH_4)_6Mo_7O_{24} \cdot 4H_2O$, were obtained from commercial sources.

For the synthesis of $Cu_3Mo_2O_9$, 2.4195 g (0.01 mmol) $Na_2MoO_4 \cdot 2H_2O$ was dissolved in 50 mL deionized water to form a transparent solution. Then, 2.4160 g (0.01 mmol) $Cu(NO_3)_2 \cdot 3H_2O$ was dissolved in 10 mL deionized water to reach a dark blue solution, which was added to the first solution dropwise by a burette and stirred at room temperature for 30 min. After stirring, the beaker was subjected to 80 W cm^{-2} ultrasonic radiation under air for 30 min using an ultra sonicator operating at 40 kHz. The reaction was carried out in a glass balloon, which was heated in an oil bath at about 100 °C for 20 h. The balloon was connected to a reflux condenser system open to the atmosphere. Next, the resulted particles were filtered and washed several times with distilled water and ethanol and then dried in an oven at a temperature of 75 °C for 3 h. The obtained powders were treated under air at temperatures ranging from 25 °C to 400 °C for 2 h and were then remained at this temperature for 4 h. Finally, $Cu_3Mo_2O_9$ was prepared as a brown-orange powder.

For the preparation of $CuMoO_4$, 5 mL of copper nitrate solution (0.50 M) was added to molybdate solution, which was obtained by dissolving 0.4414 g ammonium heptamolybdate in 50 mL deionized water (pH = 4.7). The mixture was stirred about 15 min, and then a citric acid (CA) solution in a molar proportion of 3 : 1 CA : cation was added. By evaporating the homogeneous solution at 90 °C (low-temperature crystallization), a sky blue gel was gradually formed. The obtained gel was transferred to a highly porous Prussian blue matrix at 120 °C for 24 h; then, it was calcined over a wide range of temperatures and times as shown in Fig. 2 to optimize its surface area, crystallinity and photocatalytic activity.[64] Finally, a green yellowish powder that was obtained at the end of the process was characterized.

2.2. Electrode fabrication

For electrochemical studies, working electrodes were prepared by the electrophoretic method. Two 1 × 5 cm^2 pieces of commercial stainless steel with a separation distance of 2 cm were inserted into a mixture, which was prepared by dispersing 0.0056 g of the prepared samples in 5 mL ethanol and five-minute exposure under 50 kHz ultrasonic waves. A potential of 20 V was applied between the two electrodes for 60 s. Next, the prepared electrodes were dried at 80 °C for 3 h and finally at 400 °C for 15 min.

2.3. Material characterization

XRD pattern of $CuMoO_4$ and $Cu_3Mo_2O_9$ samples were recorded on an XPERT-PRO powder X-ray diffractometer. The CuKα (k = 1.5406 and 1.5443 Å) radiation was used, and diffractions were measured over 2θ range of 5–80°. Transmission electron microscopy (TEM) images were obtained with a CM120 electron microscope from Philips. The diffuse reflectance spectra were determined with a UV-Vis spectrophotometer Avantes (Avaspec-2048-TEC) with $BaSO_4$ as the standard reference. The magnetic properties were measured using a vibrating sample magnetometer (VSM) system (Lake Shore7404).

2.4. Electrochemical characterization

All electrochemical measurements on the surface of catalysts were conducted in a 0.1 M NaOH (pH = 13) solution by a standard three-electrode cell containing Ag/AgCl as the reference electrode, a platinum mesh as the auxiliary electrode and an electrophoretically deposited material electrode as the working electrode using a Solartron SI-1260 electrochemical interface. For Mott–Schottky analysis, a Solartron Phase Gain Analyzer SI1260 was used to determine electrochemical impedance spectra (EIS) by handling a frequency of 10 000 Hz, an AC voltage amplitude of 10 mV in different scanning potential ranges for the deposited electrode *vs.* Ag/AgCl (between −0.35 and 0.2 V for $CuMoO_4$, and between −0.45 and 0.4 V for $Cu_3Mo_2O_9$) both in the dark and under illumination by a fluorescent lamp. A range of frequencies between 0.1 and 100 000 Hz was used in EIS measurements with a 10 mV amplitude perturbation.

The electrocatalytic activities of the working electrodes were tested using Cyclic Voltammetry (CV) and Linear Sweep Voltammetry (LSV), at a scan rate of 10 mV s^{-1} in different potential ranges. All electrochemical tests were performed at ambient temperature and pressure. To reduce the additional ohmic resistance, bubbles that were generated on the electrode surface under OER and HER were dispersed by stirring the solution at 1000 rpm during the reaction. Moreover, to enhance the mass transport of CO_2 during the electroreduction, CO_2 was continuously bubbled.

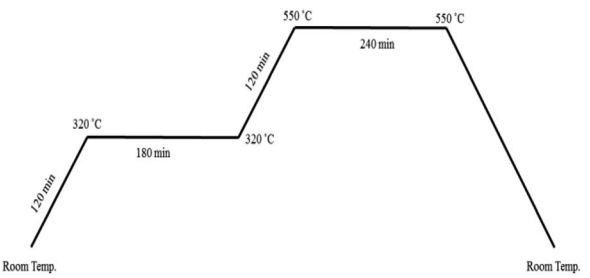

Fig. 2 Temperature profile for calcination process.

3. Results and discussion

3.1. XRD analysis

As shown in Fig. 3a, the XRD patterns of the as-prepared $CuMoO_4$ and $Cu_3Mo_2O_9$ samples reveal their crystalline nature, which are consisted of a single-phase and orthorhombic $Cu_3Mo_2O_9$ with space group $Pna2_1$ and anorthic $CuMoO_4$ with space group $P\bar{1}$. As shown, the broadening of the diffraction

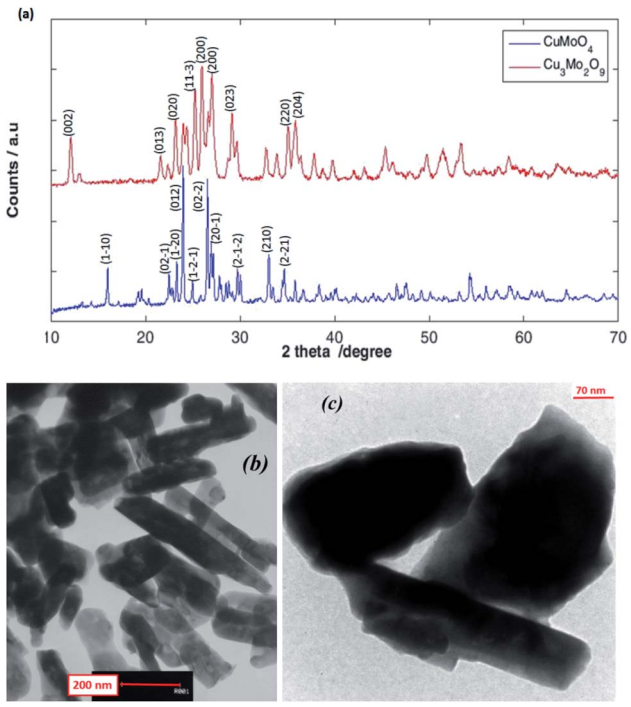

Fig. 3 (a) XRD patterns, and TEM images for (b) $Cu_3Mo_2O_9$ and (c) $CuMoO_4$.

peaks proves the high purity as well as the nanocrystalline nature of the as-prepared samples. The strong sharp diffraction peaks indicate that the samples are well crystallized. The peaks can be indexed to orthorhombic $Cu_3Mo_2O_9$ (JCPDS 94-0728)[60] and anorthic $CuMoO_4$ (JCPDS 98-000-7372).[59] The strong peaks at the defined 2θ values of 25.96, 27.02 and 25.24 can be indexed to (002), (140) and (131) planes of $Cu_3Mo_2O_9$, and at 2θ values of 23.95, 26.53 and 27.16 to (012), (201) and (211) planes of $CuMoO_4$ respectively. The (002) and (012) reflection peaks were used for the calculation of the crystallite size of $Cu_3Mo_2O_9$ and $CuMoO_4$, respectively. The average crystallite size calculated using the Debye–Scherrer equation from the FWHM (full-width half maxima) of the XRD peaks of $Cu_3Mo_2O_9$ and $CuMoO_4$ samples were found to be approximately 49 and 134 nm, respectively.

3.2. TEM

TEM studies provide further insight into the nanostructure and topography of the treated samples. Fig. 3b and c shows the TEM images of $Cu_3Mo_2O_9$ and $CuMoO_4$ for the formation of rod-shaped orthorhombic and multiform shape particles of the samples; both monocrystalline particles have diameters that are in good agreement with the size obtained from powder XRD. The nanoparticles are a little agglomerated.

3.3. Magnetic properties analysis

The relationships between the magnetization (M) and magnetic field (F) of $Cu_3Mo_2O_9$ and $CuMoO_4$ nanoparticles was determined by a vibrating sample magnetometer (VSM) system (Lake Shore 7404). Fig. 4a shows the M–F curve in the range from −18 to 18 kG with a saturated magnetization. A linear increment above 7 kG with a narrow hysteresis loop occurs between −2 and 2 kG; this pattern is the characteristic of both ferromagnetic and antiferromagnetic interactions for both samples.[65,66]

3.4. Optical properties

The optical properties of the samples were measured by UV-Vis DRS spectrum. Fig. 4b demonstrates the DRS spectra of the prepared $Cu_3Mo_2O_9$ and $CuMoO_4$ samples. Two sequential absorption bands can be identified in these samples. One band is located above 600 nm, and the other one below 600 nm; these results are in good agreement with the color of the samples. The former can be mainly attributed to d–d transition of Cu^{2+} ions ($3d^9$), whereas the latter may be due to the Cu(3d) ← O(2p) LMCT or Mo(4d) ← O(2p) LMCT and an Mo(4d) ← Cu(3d) MMCT, which is located at wavelengths higher than LMCT band.[66,67]

The direct and indirect optical band gaps of nanoparticles were extracted according to Tauc's equation.[68,69] According to Tauc's equation, the relation between the absorption coefficient (α) and the incident photon energy ($h\nu$) can be written as:

$$(\alpha h\nu)^{1/n} = A(h\nu - E_g) \quad (1)$$

where A is a constant, E_g is the band gap energy of the materials; the exponent n depends on the transition type and is equal to

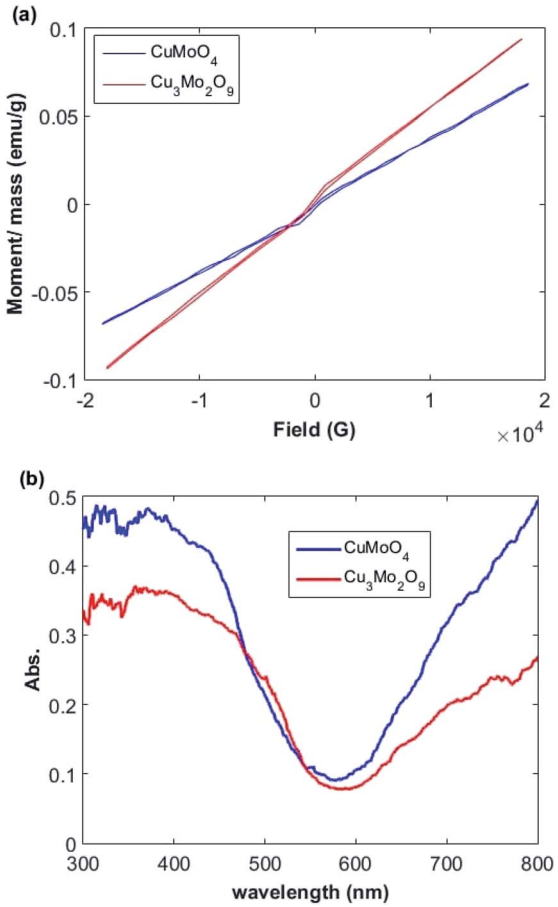

Fig. 4 (a) Magnetization curves and (b) UV-Vis diffuse reflectance spectra of $Cu_3Mo_2O_9$ and $CuMoO_4$.

0.5 and 2 for direct and indirect transitions, respectively.[70] To determine the possible transitions, $(\alpha h\nu)^{1/n}$ was plotted *versus* $h\nu$, and the corresponding band gaps were obtained by extrapolating the steepest part of the graph on the $h\nu$ axis for $(\alpha h\nu)^{1/n} = 0$. The direct and indirect band gap energies were obtained from, respectively, $(\alpha h\nu)^2$ and $(\alpha h\nu)^{1/2}$ *vs.* $h\nu$ as shown in Fig. S1.†

The larger band gaps of both samples correspond to the direct electronic transition between the upper edge of O:2p valence band and the lower edge of Mo:4d conduction band. The calculated band gaps for these transitions are 2.4 and 2.6 eV for $Cu_3Mo_2O_9$ and $CuMoO_4$, respectively. The lower energy indirect transitions can be explained by assuming the existence of narrow band correlated-electron states in the band gap instead of a single wide band of uncorrelated-electron states that may correspond to Cu^{2+}:$3d^9$ band. We speculate that in addition to the contribution of Cu (3d) on the top of O (2p) valence band, the conduction band of both samples contain Cu (3d) characteristic, in agreement with our experimental observations. The Jahn–Teller distortion of Cu^{2+} gives rise to a d-orbital splitting in which the degeneracy of σ-antibonding orbitals is broken.[38] The calculated Tauc's plot indirect band gaps are 2.1 and 2.3 eV for $Cu_3Mo_2O_9$ and $CuMoO_4$ samples, respectively, so their absorption edges are in the visible range of the spectrum. Ansari *et al.* reported that the electronic

transitions of $CuMoO_4$ are of indirect type and a band gap of 3.06 eV was obtained,[71] whereas values of 2.38, 2.80 and 2.15 eVs were obtained by other researchers.[72–74] Moreover, Dutta *et al.* found an indirect band gap of 2.32 eV.[54]

3.5. Mott–Schottky analysis

For Mott–Schottky analysis, one has to select a range of potentials in which Faraday's reaction does not occur. To determine this range, cyclic voltammetric technique was used. The characteristic of Faraday's processes is the evolution of peaks in cyclic voltammograms. For non-faradic or capacitive processes, no peak is observed and the voltammogram is almost rectangular. Cyclic voltammograms with a scan rate of 10 mV s^{-1} in potential ranges between 0.2 and −0.35 for $CuMoO_4$ and between 0.25 and −0.45 V for $Cu_3Mo_2O_9$ in 0.1 M NaOH were obtained. In this way, a range of potentials was determined over which the cyclic voltammograms showed no faradic current, and only a capacitive current was observed. In order to ensure that the observed behavior in the voltammograms was capacitive, the effect of different scan rates on the voltammograms was evaluated. If the observed behavior is capacitive, the anodic and cathodic currents should increase with increasing the scan rate. Therefore, the performance of samples in these potential regions can be considered as capacitive, as shown in Fig. S2.†

When a semiconductor is exposed to an electrolyte, it reaches the thermodynamic equilibrium with the electrolyte by exchanging electrons through the interface and adjusting the Fermi level of the semiconductor to the Fermi level of the electrolyte, which results in the formation of a space charge layer. The Fermi level position of the electrolyte is constant because the number of available states in the electrolyte solution is typically more than the number of states in the semiconductor. With regard to electron transfer from/to a semiconductor to/from an electrolyte, an excess of immobilized charge in the semiconductor and an excess of opposite charge in the electrolyte are produced just behind the interface and in the space charge layer. This implies that the energy bands are bent,[75] and the amount of bending depends on the difference between band edge energy in the semiconductor and at the interface; furthermore, the amount of bending corresponds to the potential drop in the space charge layer, U_S. When an external electrical source is applied, then $U_S = U_{app} - U_{FB}$, where U_{FB} is the flat band potential, that is, a unique potential for which the potential drop between the bulk and surface is zero. Thus, by determining the flat band potential one can estimate the situations of conduction and valence band edges for n-type and p-type semiconductors, respectively.[76] Mott–Schottky theory describes the properties of semiconductor electrolyte interface using space charge capacitance as follows[77–79]

$$\frac{1}{{C_{SC}}^2} = \frac{2}{qN\varepsilon\varepsilon_0}\left(U_{FB} - U_{app} - \frac{kT}{e}\right) \quad (2)$$

where ε is the relative permittivity of the semiconductor, ε_0 is the vacuum permittivity and is equal to 8.85×10^{-12} F m^{-1}; q is the elementary charge (-1.6×10^{-19} C for electrons and $+1.6 \times 10^{-19}$ for holes), N is the carrier charge concentration, U_{app} is the applied potential, U_{FB} is the flat band potential, T is the absolute temperature and k is the Boltzmann's constant and is equal to 1.381×10^{-23} J K^{-1}. The latest term in eqn (2), kT/e = 0.026 V at 300 K, is small and can be omitted. CSC can be calculated from impedance as, $C_{SC} = (-1)/(2\pi\nu Z_j)$ where ν is the frequency and Z_j is the imaginary part of the impedance. Fig. 5a and b shows Mott–Schottky plots for both samples at a frequency of 10 000 Hz in 0.1 M NaOH in the dark and under illumination.

A fairly large frequency of 10 000 Hz is chosen since fast processes such as charging of double layer and space charge layer capacitors respond at this frequency. Obviously, selecting and recognizing the linear region are difficult. Therefore, since at this frequency, the samples exhibit capacitive behavior and the capacity of the space charge layer is independent of potential, the Nyquist diagrams are in a range of potentials selected from the CVs. It is expected that these diagrams will coincide almost exactly with the region where only the space layer charging occurs.

For this purpose, Nyquist diagrams with 0.05 V potential interval and over a frequency range of 0.1 to 100 000 Hz are plotted in the dark and under illumination in 0.1 M NaOH solution (Fig. S3 and S4†). As illustrated in these figures, Nyquist diagrams over the range −0.24 to −0.12 V for $CuMoO_4$ and the range −0.30 to −0.18 V for $Cu_3Mo_2O_9$ in the dark are fairly in good agreement. Therefore, these regions were used for the linear fitting of the Mott–Schottky equation, and the results are shown in Fig. S5 and S6.† A correlation coefficient close to 1

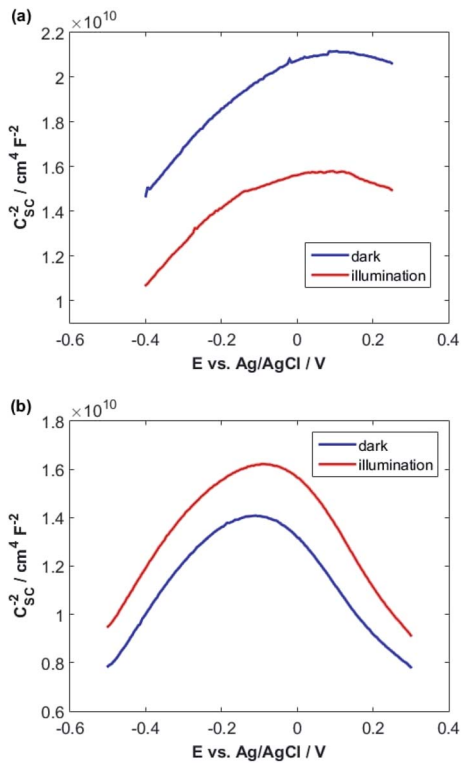

Fig. 5 Mott–Schottky plots both in the dark and under illumination for (a) $CuMoO_4$ and (b) $Cu_3Mo_2O_9$.

implies a good agreement between the experimental results and the results of the Mott–Schottky theory. The value of U_{FB} can be determined from the intercept of the fitting line with the Mott–Schottky plot. In Fig. S5 and S6,† the slopes of Mott–Schottky plots for both electrodes are positive; this confirms that the electrodes are n-type semiconductors, and consequently, the lower conduction band edge practically merges with the quasi-Fermi level of electrons. The conduction band edge, E_C, can be experimentally estimated using flat band potential (U_{FB}).[80] For this propose, the electrochemical potentials should be related to absolute energy, E_{abs}, and the effects of pH should be considered using the following equations at 25 °C:

$$E_{RHE}\ (V) = E_{Ag/AgCl} + 0.199 + 0.0592pH \quad (3)$$

$$E_{abs}\ (eV) = -4.5 - E_{RHE} \quad (4)$$

where E_{RHE} and $E_{Ag/AgCl}$ are potentials against the reversible hydrogen electrode and Ag/AgCl reference electrode, respectively.

As can be seen, different values were obtained for the flat band potentials for both samples. The values of E_C for both samples were determined using the U_{FB} values reported in Table 1 and eqn (3) and (4).

Then, with a method, which has already been described in the electrochemical studies of nanostructured nickel titanate[81] and benefits from a combination of optical (DRS) and electrochemical (impedance) spectroscopies, we determined the valence band edges, E_V, of both samples with subtracting the values of band gap energies from E_C. All band edges for both samples are reported in Table 1 for in the dark and under illumination. According to these data, we outline the experimental electronic band structures of both samples as illustrated in Fig. 6. The O^{2-}:2p and Cu^{2+}:3d orbitals contribute to the valence band; additionally, O^{2-}:2p and Mo^{6+}:4d orbitals contribute to the conduction band for both compounds.[82]

The density of donor atoms can be calculated using the slope value of Mott–Schottky plots (Fig. S5 and S6†) and eqn (2). The calculated values are shown in Table 1. The density of donor atoms, especially copper atoms, in $Cu_3Mo_2O_9$ is larger than $CuMoO_4$. Moreover, using N_D values, it is possible to estimate the diffusion length of minor charge carriers (here holes) using the following equations at 25 °C:

$$L = \left(\frac{\varepsilon\varepsilon_0\, kT}{q^2 N_D}\right)^{\frac{1}{2}} \quad (5)$$

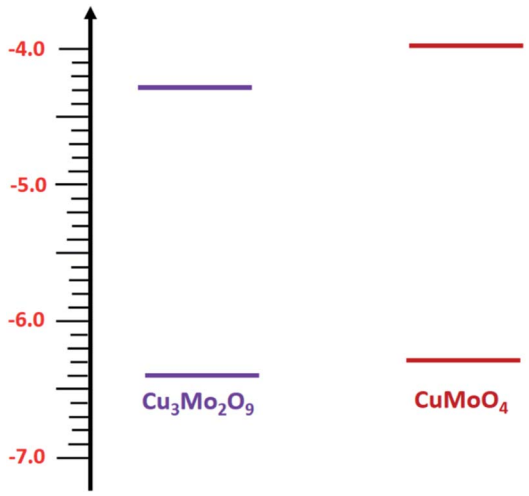

Fig. 6 Energy states diagram of $CuMoO_4$ and $Cu_3Mo_2O_9$.

$$W_D = \left(\frac{2\varepsilon\varepsilon_0\, kT}{q\, N_D}\right)^{\frac{1}{2}}\left(U_{app} - U_{FB} - \frac{kT}{q}\right) \quad (6)$$

The obtained results are shown in Table 1 considering that the dielectric constants of $Cu_3Mo_2O_9$ and $CuMoO_4$ are equal to 7.2 (ref. 83) and 7.9,[84] respectively.

One can calculate diffusion length of minority carrier, L, and the thickness of the depletion layer, W_D, by using U_{FB}, N_D and eqn (2). The values of N_D, L and W_D (for $U_{app} - U_{FB} = 1$ V) were computed, and the results (accompanied with U_{FB}) are listed in Table 1.

3.6. Electrochemical water splitting studies

Electrochemical water splitting includes oxygen evolution reaction, OER, on the anode surface and hydrogen evolution reaction, HER, on the cathode surface. Electrochemical water splitting is a pH-dependent reaction, so it has been widely investigated in both acidic and alkaline solutions. From the technological viewpoint, Schalenbach *et al.* showed that alkaline water electrolyzers are more efficient compared to acidic ones.[85] Moreover, from the electrocatalyst design viewpoint, alkaline solutions allow us to use earth-abundant materials, especially for OER,[86,87] whereas acidic solutions are limited to precious metals and metal oxides.[88] However, the big disadvantage of alkaline solutions is the sluggish kinetics of OER in these media.[89]

Table 1 Some calculated parameters using Mott–Schottky analysis for both $CuMoO_4$ and $Cu_3Mo_2O_9$ samples

Sample	Condition	U_{FB}/V	N_D/cm^{-3}	W_D/cm	L/cm	E_C *vs.* NHE/V	E_C (abs)/eV	E_C (abs)/eV	E_g/eV
$CuMoO_4$	Dark	−1.50	1.25×10^{21}	8.36×10^{-8}	9.44×10^{-9}	−0.53	−4.0	−6.3	2.3
	Illumination	−1.29	1.38×10^{21}	7.95×10^{-8}	9.02×10^{-9}	−0.32	−4.2	−6.5	2.3
$Cu_3Mo_2O_9$	Dark	−1.18	1.42×10^{21}	7.48×10^{-8}	8.49×10^{-9}	−0.21	−4.3	−6.4	2.1
	Illumination	−1.36	1.47×10^{21}	7.36×10^{-8}	8.34×10^{-9}	−0.39	−4.1	−6.2	2.1

This is due to the four-electron-proton transfer mechanism in alkaline media, which is the rate-determining step at high overpotentials. Therefore, to compare $CuMoO_4$ and $Cu_3Mo_2O_9$ in electrochemical OERs, one should calculate their potentials and kinetic parameters such as exchange current density and Tafel slope. The overall reaction, which occurs on the surface of the electrocatalyst is:

$$4OH^- + 4h_{VB}^+ \rightarrow 2H_2O + O_2 \quad (7)$$

During this complex reaction, four electrons are transferred to the valence band of the semiconductor. As shown in Fig. 6, it is expected that the injection of the electrons of OH^- to the valence band of $Cu_3Mo_2O_9$ is more favorable compared to that of $CuMoO_4$ because of its lower E_V, and consequently, a higher OER activity than $CuMoO_4$. Fig. 7a shows the comparative LSVs of both samples for OER measured in 0.1 M NaOH solution at 25 °C; they indicate close onset potentials. The dashed line shows the standard potential of OER. As Fig. 7a shows, OER overpotentials of 0.28 and 0.42 V at a current density of 1 mA cm^{-2} were obtained for nanostructured $Cu_3Mo_2O_9$ and $CuMoO_4$, respectively. These results are in agreement with the diagram of Fig. 6. In addition, these numerical values are in good agreement with the results of Gou *et al.*, who reported an overpotential of 0.325 mV at 50 mA cm^{-2} in 1.0 M KOH for $Cu_3Mo_2O_9$ nanosheet loaded on nickel foam.[90]

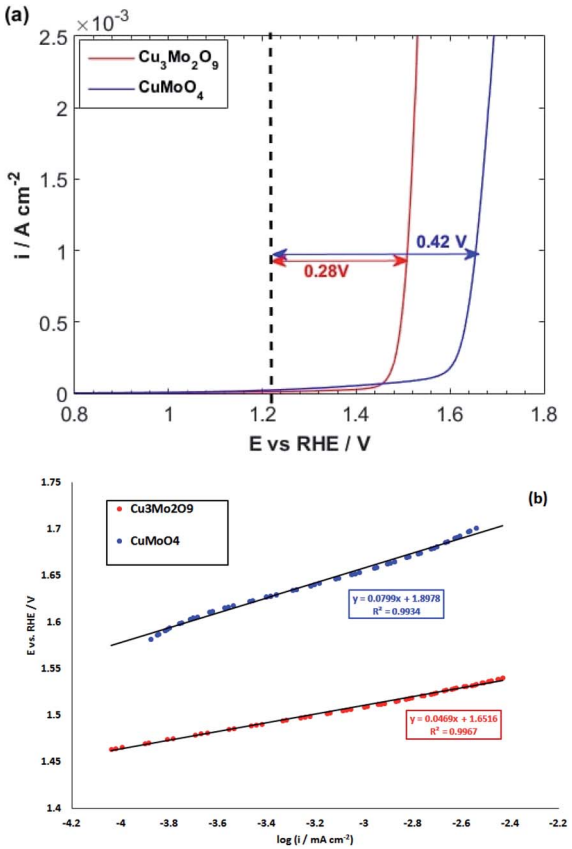

Fig. 7 (a) LSVs and (b) linear parts of polarization curves of $CuMoO_4$ and $Cu_3Mo_2O_9$ for OER with a scan rate of 10 mV s^{-1} in 0.1 M NaOH.

The kinetics of OER at electrode interfaces were reflected by their corresponding polarization curves. The linear curve fitting gives the Tafel slopes of 46.9 and 79.9 mV dec^{-1} for, respectively, $CuMoO_4$ and $Cu_3Mo_2O_9$, as illustrated in Fig. 7b. These slopes are less than that of Pt/C (99 mV dec^{-1}), indicating a more rapid kinetics for OER on the surfaces of these electrocatalysts compared to Pt/C.[91]

The obtained Tafel slopes are close to those reported for some nickelates and cobaltates by Bockris and Otagawa,[92] who investigated OER on the surface of different perovskites and developed a common mechanism for OER by emphasizing on electrochemical adsorption of OH^- ions followed by desorption of OH and formation of H_2O_2 as an intermediate that is decomposed into O_2. Such a mechanism has also been suggested for RuO_2 (ref. 93) and TiO_2.[94] Scheme 1 was inspired by their work.

Mott–Schottky analysis showed that Cu^{2+} ions are the localized charges in the space charge layer, thus they should be involved in interfacial phenomena. Accordingly, for the adapted mechanism, we supposed that the adsorption of OH^- ions occurs on the copper ions. The first step in Scheme 1 is the formation of the adsorbed OH radicals, which can occur *via* discharging of both hydroxyl ions and H_2O molecules. However, in alkaline solution, hydroxyl ions reach the surface of electrodes faster than water molecules because of their diffusion coefficient.[95,96] The second step, which is rds, includes the electrochemical desorption of OH radicals, the formation of physically adsorbed hydrogen peroxide and OH^- vacancy on the surface of these compounds. The next two steps are fast steps and show desorption and decomposition of hydrogen peroxide and the formation of O_2 molecules. The final fast step is surface diffusion of OH^- into the oxygen vacancy sites. The exchange current densities (i_0) (measured by extrapolation of the Tafel

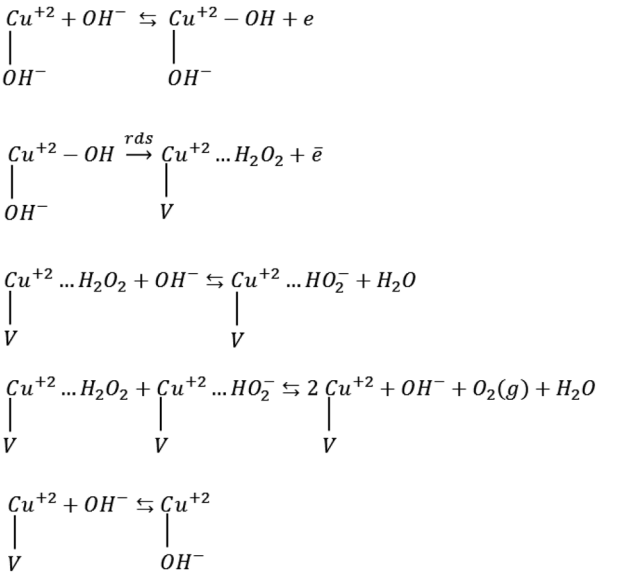

Scheme 1 OER mechanism by emphasizing on the electrochemical desorption of OH^- as the rate-determining step (rds). V denotes an OH^- vacancy and dots show physisorbed species.

plot) were calculated, and the values of 6.8×10^{-10} and 3.1×10^{-9} mA cm^{-2} were obtained for $CuMoO_4$ and $Cu_3Mo_2O_9$, respectively. Generally, the exchange current density is expected to be proportional to the surface density of catalytically active sites; here, Cu^{2+} ions correspond to the below mechanism.

After investigating the OER activity, the electrocatalytic performances of the samples were comparatively studied in terms of HER in 0.1 M NaOH solution at 25 °C. For this purpose, the LSVs of both samples were taken by starting from positive potentials to negative potentials up to the occurrence of HER, which is identified by a sharp increase in cathodic current. The resulting LSVs are depicted in Fig. 8a. It is observed that some cathodic peaks exist before hydrogen evolution. Liu *et al.* showed that the redox reaction of Mo in copper molybdate does not occur during electrochemical measurement, so the redox behavior of Mo has no contribution to the measured capacitance.[97] Moreover, our previous study on the comparative electrochemical behaviors of $CuWO_4$ and CuO showed that these peaks can be attributed to Cu(II)/Cu(I) and Cu(I)/Cu(0) redox reactions.[64] Cyclic voltammograms (Fig. S7†) show more detail on these redox reactions for both samples. These cyclic voltammograms clearly show that the reduction of copper ions to copper atoms occurs before HER. Therefore, HER occurs on the surface of molybdate-derived copper atoms. In fact, HER takes place in acidic media more facile than in alkaline solution. However, using acidic electrolyte has some disadvantages, such as the corrosion of the electrolyzer.[98]

Moreover, the reaction needs more energy to produce proton by O–H bond cleavage of water molecules in alkaline solution.[99] The elementary steps for HER in alkaline solution accompanied by their Tafel slopes are:

Volmer step (120 mV dec^{-1}):

$$H_2O + M + e \rightarrow M\text{–}H + OH^- \quad (8)$$

Heyrovsky step (40 mV dec^{-1}):

$$H_2O + M\text{–}H + e \rightarrow M + H_2 + OH^- \quad (9)$$

Tafel step (30 mV dec^{-1}):

$$M\text{–}H + M\text{–}H \rightarrow 2M + H_2 \quad (10)$$

Based on these steps, two mechanisms of Volmer–Heyrovsky and Volmer-Tafel are possible. The Volmer step, which is the water dissociation step, is common in both mechanisms. The energy required for this step can be provided by the adsorption of water molecules on the surface of the electrocatalyst.[100] The stronger the water molecules adsorption the more the energy provided for the Volmer step. In addition, adsorption of OH^- ions on the active sites has a poisoning effect and increases the overpotential by lowering the activity because of limiting the number of sites in alkaline solution. The hydrogen binding energy is another important factor that governs the HER activity of the catalysts. In fact, a volcano-type correlation between HER exchange current densities and H-binding energy values was demonstrated, which was supported by both DFT and experimental studies.[101,102] Furthermore, the crystallographic planes

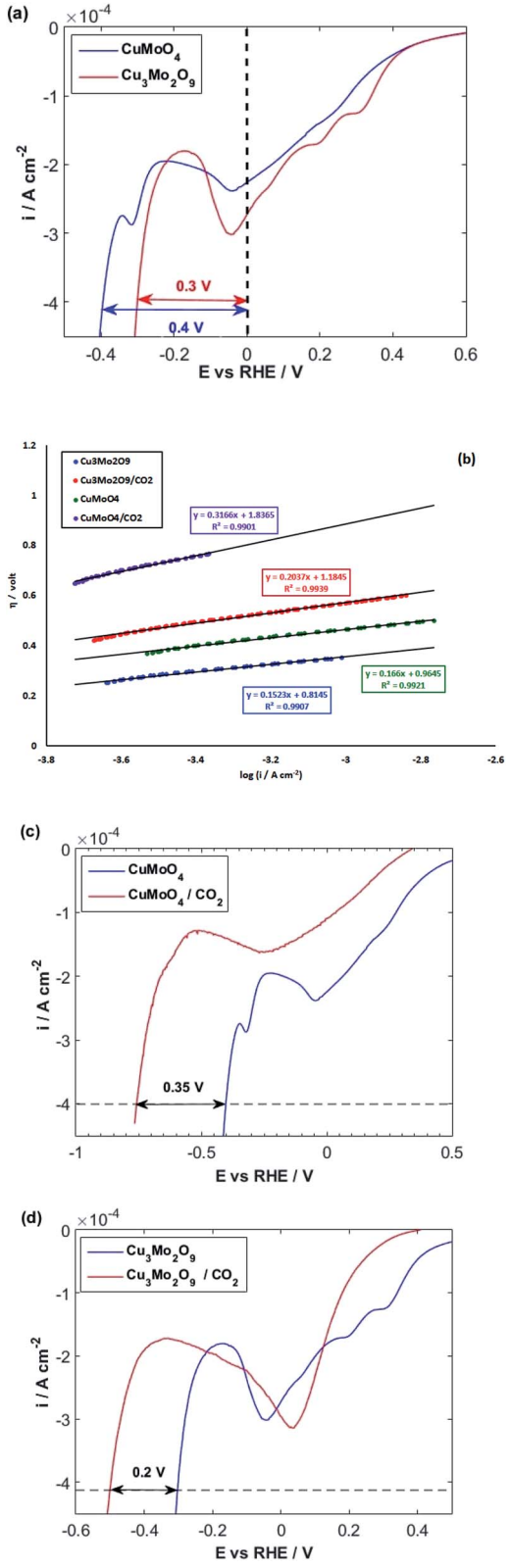

Fig. 8 (a) LSVs and (b) linear parts of polarization curves of $CuMoO_4$ and $Cu_3Mo_2O_9$ for OER with a scan rate of 10 mV s^{-1} in 0.1 M NaOH and (c and d) polarization curves of $CuMoO_4$ and $Cu_3Mo_2O_9$ in the presence/absence of CO_2.

of the catalysts[103] and the existence of an active component for water dissociation[104] can affect the kinetics of the reaction.

As illustrated in Fig. 8a, the HER overpotential on the surface of $Cu_3Mo_2O_9$ has a value of around 0.1 V, which is smaller than that of $CuMoO_4$ at a current density of 0.4 mA cm^{-2}. Because the adsorbed molecules (here, water) and the active sites (here, copper atoms) are the same in nature, the predominant factor should be the number of active sites. It is clear that the surface density of copper atoms on the surface of $Cu_3Mo_2O_9$ is larger than that of $CuMoO_4$, so more surface sites are available for HER on the surface of $Cu_3Mo_2O_9$; this lowers the overpotential. Moreover, although a precise look indicates copper active sites, copper atoms have different arrangements and different sublayers. Reduction of copper ions to copper occurs on the surface layer of copper molybdates, and the oxygen species, which exist in the sublayers, facilitate water molecules adsorption, causing HER promotion.[105,106] Our previous work on the comparative studies of $CuWO_4$ and CuO showed that the sublayer atoms have a considerable effect on lowering HER overpotentials.[64] The effects of the nature of sublayer atoms and their configurations on reducing the HER overpotential on the surface of copper were already reported by Zhang *et al.*; they investigated full water splitting on sulfur-doped copper oxide in comparison with metallic copper.[107]

Fig. 8b shows a Tafel slope close to 120 mV dec^{-1} for both samples highlighting that the Volmer step is the rate-determining step in HER mechanism for both samples. The Tafel slopes of 166 and 152 mV dec^{-1} were obtained, and accordingly, exchange current densities of 1.5×10^{-6} and 4.5×10^{-6} A cm^{-2} were calculated for $CuMoO_4$ and $Cu_3Mo_2O_9$, respectively. It means that the rate of HER on the surface of $Cu_3Mo_2O_9$ is three times faster compared to $CuMoO_4$, which can be expected because of the more accessible active sites of this compound. The number of surface sites was also used for identifying the smaller Tafel slope for HER on the surface of MoS_2.[108,109] Additionally, these results are in agreement with our previous findings that compared $CuWO_4$ and CuO.[64] We showed that exchange current density for HER on the surface of CuO is much larger than that of $CuWO_4$. Similarly, as shown in Fig. 1, the structural difference between $CuMoO_4$ and $Cu_3Mo_2O_9$ is that the latter has one CuO unit for each $CuMoO_4$ pair, *i.e.*, $Cu_3Mo_2O_9 \equiv 2CuMoO_4 + CuO$, and because of the existing CuO unit, $Cu_3Mo_2O_9$ has a larger exchange current density.

At the final step of our electrochemical studies, we investigated the ability of both samples for CO_2 reduction. Therefore, we purged the 0.1 M NaOH solution with CO_2 for at least 30 min. The pH of the solution decreased from 13 to around 7 because of the following equilibrium:

$$OH^-(aq) + CO_2(aq) \leftrightarrows HCO_3^-(aq) \quad (11)$$

$$OH^-(aq) + HCO_3^-(aq) \leftrightarrows CO_3^{2-}(aq) \quad (12)$$

At ambient temperature and natural pH, the major species inside the solution is HCO_3^-.[110] Fig. 8c and d illustrate that HER takes place in more negative potentials when CO_2 is bubbled into the solution, and consequently, CO_2 and its related species HCO_3^- and CO_3^{2-} are present in the solution, *i.e.*, the HER overpotential increases for both samples.

For investigating this process in more detail, we compared the cyclic voltammograms of both compounds with and without CO_2 bubbling. The results are presented in Fig. S8.†

Both cathodic and anodic peaks of the samples in CO_2 saturated 0.1 M NaOH solution show a significant decrease in height. This indicates that the adsorption of CO_2 and maybe its reduction intermediates occur on the same sites where HER occurs. Furthermore, the adsorption of CO_2 has a poisoning effect on HER and inhibits it.

In fact, there is a competition between H_2O and CO_2 molecules to be reduced on the surface of copper atoms.[111,112] However, according to Fig. 8c and d, when CO_2 is blown into the NaOH solution, the increasing of HER overpotential for $CuMoO_4$ is more than that of $Cu_3Mo_2O_9$ by around 0.15 V.

It means that the dissolved CO_2 species in the solution or the adsorbed CO_2 reduction intermediates occupy more HER active sites on the surface of $CuMoO_4$ compared to $Cu_3Mo_2O_9$. This implies the fact that the density of active sites (here, copper atoms) on the surface of $Cu_3Mo_2O_9$ is higher compared to $CuMoO_4$. Moreover, the atoms and their configuration in the sublayer have a considerable effect on the adsorption of CO_2.

The Tafel slope analysis for HER in the presence of CO_2 shows the same value of exchange current density of 1.5×10^{-6} A cm^{-2}, for both samples, whereas $Cu_3Mo_2O_9$ has a larger surface density of active sites for HER. Actually, it is possible that when HER starts on $Cu_3Mo_2O_9$, some sites have still been occupied by CO_2 reduction species. According to our previous report,[64] which showed that, in the presence of CO_2-species in the solution, HER occurs more readily than $CuWO_4$. Therefore, it is possible here that HER occurs on the surface of copper atoms, which have come from CuO unit of $Cu_3Mo_2O_9$, while CO_2-species involved in the reaction on the surface of copper atoms have originated from $CuMoO_4$ units of $Cu_3Mo_2O_9$. This means that the adsorption of CO_2-species is strong on the surface of $CuMoO_4$.

In fact, the existence of oxygen in sublayers causes the strong adsorption of CO_2, which will produce carbon-rich CO_2-reduction products such as alcohols, carboxylic acids and hydrocarbons instead of CO. This conclusion can be supported by other reports. For instance, it has been reported that oxide-derived copper produces methanol,[113–115] ethylene and ethanol with increased current efficiency.[116] Moreover, the existence of tin oxide layer over tin effectively produces formate[117,118] and formic acid.[119] Tayyebi *et al.* used DFT calculation for electrochemical reduction of CO_2 for producing methanol, methane and formic acid over different transition metal oxides, and showed that there is a volcano-shaped behavior through the scaling relations of adsorbed intermediates.[120]

4. Conclusion

In this study, two types of copper molybdate, $CuMoO_4$ and $Cu_3Mo_2O_9$, were synthesized successfully in nanoscale. Our results showed that the difference between their electrochemical behaviors strongly depends on their crystal structure.

In fact, the existence and addition of CuO unit in the unit cell of $Cu_3Mo_2O_9$ caused a modified behavior corresponding to a combination of CuO and $CuMoO_4$.

The value of the Tafel slope for $Cu_3Mo_2O_9$ (as OER) was much lower than that for $CuMoO_4$. Therefore, $Cu_3Mo_2O_9$ shows a better catalytic performance for both HER and OER in 0.1 M alkaline solution. The literature review indicated that $Cu_3Mo_2O_9$ could be a bifunctional water splitting catalyst under alkaline conditions, and show better activity at low cell voltage than $CuMoO_4$. The superior OER and HER activities for $Cu_3Mo_2O_9$ can be attributed to the more active sites arising from oxygen vacancies or the unique topology of $Cu_3Mo_2O_9$ crystals that maximizes the number of exposed active sites. However, our investigation showed that CO_2-species are adsorbed on the surface of $CuMoO_4$ more strongly than on the surface of $Cu_3Mo_2O_9$, so they may produce more stable and carbon-rich products.

Conflicts of interest

There are no conflicts to declare.

Acknowledgements

Authors acknowledge the financial support from University of Birjand.

References

1 A. Sivanantham, P. Ganesan and S. Shanmugam, *Adv. Funct. Mater.*, 2016, **26**, 1–8.
2 X. Xu, Y. Ge, M. Wang, Z. Zhang, P. Dong, R. Baines, M. Ye and J. Shen, *ACS Appl. Mater. Interfaces*, 2016, **8**, 18036–18042.
3 K. Maeda and K. Domen, *J. Phys. Chem. Lett.*, 2010, **18**, 2655–2661.
4 K. Maeda, *J. Photochem. Photobiol., C*, 2011, **12**, 237–268.
5 X. Zou and Y. Zhang, *Chem. Soc. Rev.*, 2015, **44**, 5148–5180.
6 S. N. Lou, J. Scott, A. Iwase, R. Amal and Y. H. Ng, *J. Mater. Chem. A*, 2016, **4**, 6964–6971.
7 J. Bisquert and S. Giménez, *Photoelectrochemical Solar Fuel Production*, Springer, Switzerland, 2016.
8 K. Maeda, *Phys. Chem. Chem. Phys.*, 2013, **15**, 10537–10548.
9 Y. Tachibana, L. Vayssieres and J. R. Durrant, *Nat. Photonics*, 2012, **6**, 511–518.
10 M. Kitano and M. Hara, *J. Math. Chem.*, 2010, **20**, 627–641.
11 E. Nurlaela, S. Ould-Chikh, M. Harb, S. del Gobbo, M. Aouine, E. Puzenat, P. Sautet, K. Domen, J.-M. Basset and K. Takanabe, *Chem. Mater.*, 2014, **26**, 4812–4825.
12 A. Fujishima and K. Honda, *Nature*, 1972, **238**, 37–38.
13 G. A. Olah, G. K. S. Prakash and A. Goeppert, *J. Am. Chem. Soc.*, 2011, **133**, 12881–12898.
14 H. Arakawa, M. Aresta, J. N. Armor, M. A. Barteau, E. J. Beckman, A. T. Bell, J. E. Bercaw, C. Creutz, E. Dinjus, D. A. Dixon, K. Domen, D. L. DuBois, J. Eckert, E. Fujita, D. H. Gibson, W. A. Goddard, D. W. Goodman, J. Keller, G. J. Kubas, H. H. Kung, J. E. Lyons, L. E. Manzer, T. J. Marks, K. Morokuma, K. M. Nicholas, R. Periana, L. Que, J. Rostrup-Nielson, W. M. H. Sachtler, L. D. Schmidt, A. Sen, G. A. Somorjai, P. C. Stair, B. R. Stults and W. Tumas, *Chem. Rev.*, 2001, **101**, 953–996.
15 B. C. Brodie, *Proceedings of the Royal Society of London*, London, 1873–1874, vol. 22, p. 245.
16 Y. Hori, O. Koga, A. Aramata and M. Enyo, *Bull. Chem. Soc. Jpn.*, 1992, **65**, 3008–3010.
17 E. E. Benson, C. P. Kubiak, A. J. Sathrum and J. M. Smieja, *Chem. Soc. Rev.*, 2009, **38**, 89–99.
18 W. Zhu, R. Michalsky, O. N. Metin, H. Lv, S. Guo, C. J. Wright, X. Sun, A. A. Peterson and S. Sun, *J. Am. Chem. Soc.*, 2013, **135**, 16833–16836.
19 M. Watanabe, M. Shibata, A. Kato, M. Azuma and T. Sakata, *J. Electrochem. Soc.*, 1991, **138**, 3382–3389.
20 G. Kyriacou and A. Anagnostopoulos, *J. Electroanal. Chem.*, 1992, **322**, 233–246.
21 M. Watanabe, M. Shibata, A. Katoh, T. Sakata and M. Azuma, *J. Electroanal. Chem.*, 1991, **305**, 319–328.
22 M. Schwartz, R. L. Cook, V. M. Kehoe, R. C. Macduff, J. Patel and A. F. Sammells, *J. Electrochem. Soc.*, 1993, **140**, 614–618.
23 J. F. Xie, Y. X. Huang, W. W. Li, X. N. Song, L. Xiong and H. Q. Yu, *Electrochim. Acta*, 2014, **139**, 137–144.
24 C. S. Chen, A. D. Handoko, J. H. Wan, L. Ma, D. Ren and B. S. Yeo, *Catal. Sci. Technol.*, 2015, **5**, 161–168.
25 X. Guo, Y. Zhang, C. Deng, X. Li, Y. Xue, Y.-M. Yan and K. Sun, *Chem. Commun.*, 2015, **51**, 1345–1348.
26 R. S. Kumar, S. S. Kumar and M. A. Kulandainathan, *Electrochem. Commun.*, 2012, **25**, 70–73.
27 R. Hinogami, S. Yotsuhashi, M. Deguchi, Y. Zenitani, H. Hashiba and Y. Yamada, *ECS Electrochem. Lett.*, 2012, **1**, 17–19.
28 W. C. Li and M. Kanan, *J. Am. Chem. Soc.*, 2012, **134**, 7231–7234.
29 Y. Lan, C. Gai, P. J. A. Kenis and J. Lu, *ChemElectroChem*, 2014, **1**, 1577–1582.
30 Y. Lan, S. Ma, J. Lu and P. J. A. Kenis, *Int. J. Electrochem. Sci.*, 2014, **9**, 7300–7308.
31 Y. Hori, R. Takahashi, Y. Yoshinami and A. Murata, *J. Phys. Chem. B*, 1997, **101**, 7075–7081.
32 K. J. P. Schouten, Z. S. Qin, E. P. Gallent and M. T. M. Koper, *J. Am. Chem. Soc.*, 2012, **134**, 9864–9867.
33 A. Han, H. Zhang, R. Yuan, H. Ji and P. Du, *ACS Appl. Mater. Interfaces*, 2017, **9**, 2240–2248.
34 Z. Lou, Y. Li, L. Zhu, W. Xie, W. Niu, H. Song, Z. Ye and S. Zhang, *J. Mater. Chem. A*, 2017, **5**, 2732–2738.
35 Y. Kwon, A. Soon, H. Han and H. Lee, *J. Mater. Chem. A*, 2015, **3**, 156–162.
36 C. Li, J. Wang, Z. Jiang and P. Hu, *New J. Chem.*, 2015, **39**, 4562–4567.
37 D. Hu, P. Diao, D. Xu, M. Xia, Y. Gu, Q. Wu, C. Li and S. Yang, *Nanoscale*, 2016, **8**, 5892–5901.
38 K. J. Pyper, J. E. Yourey and B. M. Bartlett, *J. Phys. Chem. C*, 2013, **117**, 24726–24732.
39 J. E. Yourey and B. M. Bartlett, *J. Mater. Chem.*, 2011, **21**, 7651–7660.

40 J. Liu, S. Wen, X. Zou, F. Zuo, G. J. O. Beran and P. Feng, *J. Mater. Chem. A*, 2013, **1**, 1553–1556.
41 S. Cobo, J. Heidkamp, P. Jacques, J. Fize, V. Fourmond, L. Guetaz, B. Jousselme, V. Ivanova, H. Dau, S. Palacin, M. Fontecave and V. Artero, *Nat. Mater.*, 2012, **11**, 802–807.
42 X. Liu, H. Zheng, Z. Sun, A. Han and P. Du, *ACS Catal.*, 2015, **5**, 1530–1538.
43 T. K. Ghorai, D. Dhak, S. Dalai and P. Pramanik, *J. Mol. Catal. A: Chem.*, 2007, **273**, 224–229.
44 K. S. Makarevich, N. V. Lebukhova, P. G. Chigrin and N. F. Karpovich, *Inorg. Mater.*, 2010, **46**, 1359–1364.
45 B. Wang, K. Zhou, B. Wang, Z. Gui and Y. Hu, *Ind. Eng. Chem. Res.*, 2014, **53**, 12355–12362.
46 S. H. Qiblawi and R. L. LaDuca, *Inorg. Chim. Acta*, 2014, **413**, 115–120.
47 S. Mitchell, A. Gómez-Avilés, C. Gardner and W. Jones, *J. Solid State Chem.*, 2010, **183**, 198–207.
48 D. Du, R. Lan, W. Xu, R. Beanland, H. Wang and S. Tao, *J. Mater. Chem. A*, 2016, **4**, 17749–17756.
49 L. Zhang, T. Li, Y. Deng, Y. Zhang, S. Hu and W. Sun, *J. Iran. Chem. Soc.*, 2014, **11**, 407–414.
50 M. Benchikhi, R. E. Ouatib, S. Guillemet-Fritsch, J.-Y. Chane-Ching, L. Er-Rakho and B. Durand, *Ceram. Int.*, 2014, **40**, 5371–5377.
51 Z. Shahri, M. Salavati-Niasari, N. Mir and G. Kianpour, *J. Cryst. Growth*, 2014, **386**, 80–87.
52 J. Xia, L. X. Song, W. Liu, Y. Teng, L. Zhao, Q. S. Wang and M. M. Ruan, *Dalton Trans.*, 2015, **44**, 13450–13454.
53 J. Xia, L. X. Song, W. Liu, Y. Teng, Q. S. Wang, L. Zhao and M. M. Ruan, *RSC Adv.*, 2015, **5**, 12015–12024.
54 D. P. Dutta, A. Rathore, A. Ballal and A. K. Tyagi, *RSC Adv.*, 2015, **5**, 94866–94878.
55 W. G. Chu, H. F. Wang, Y. J. Guo, L. N. Zhang, Z. H. Han, Q. Q. Li and S. S. Fan, *Inorg. Chem.*, 2009, **48**, 1243–1249.
56 T. Ito, H. Takagi and T. Asano, *Chem. Mater.*, 2009, **21**, 3376–3379.
57 S. Hara and H. Sato, *J. Phys. Soc. Jpn.*, 2013, **82**, 054801–054805.
58 C. Canevali, F. Morazzoni, R. Scotti, D. Cauzzi, P. Moggi and G. Predieri, *J. Mater. Chem.*, 1999, **9**, 507–513.
59 S. C. Abrahams, J. L. Bernstein and P. B. Jamieson, *J. Chem. Phys.*, 1968, **48**, 2619–2629.
60 B. L. Kihlborg, R. Norrestam and B. Olivecrona, *Acta Crystallogr., Sect. B: Struct. Crystallogr. Cryst. Chem.*, 1971, **27**, 2066–2070.
61 C. F. Macrae, I. J. Bruno, J. A. Chisholm, P. R. Edgington, P. McCabe, E. Pidcock, L. Rodriguez-Monge, R. Taylor, J. van de Streek and P. A. Wood, *J. Appl. Crystallogr.*, 2008, **41**, 466–470.
62 C. F. Macrae, P. R. Edgington, P. McCabe, E. Pidcock, G. P. Shields, R. Taylor, M. Towler and J. van de Streek, *J. Appl. Crystallogr.*, 2006, **39**, 453–457.
63 I. J. Bruno, J. C. Cole, P. R. Edgington, M. K. Kessler, C. F. Macrae, P. McCabe, J. Pearson and R. Taylor, *Acta Crystallogr., Sect. B: Struct. Sci.*, 2002, **58**, 389–397.
64 H. Farsi, S. Moghiminia, M. Raygan, E. Dana, S. Hosseini, M. Behforooz, T. Zubkov, I. V. Lightcap and Z. Li, *J. Phys. Chem. C*, 2019, **123**, 25941–25948.
65 S. Vilminot, G. Andre and M. Kurmoo, *Inorg. Chem.*, 2009, **48**, 2687–2692.
66 T. Ito, H. Takagi and T. Asano, *Chem. Mater.*, 2009, **21**, 3376–3379.
67 X. Fu, J. Ji, W. Tang, W. Liu and S. Chen, *Mater. Chem. Phys.*, 2013, **141**, 719–726.
68 J. Tauc, *Mater. Res. Bull.*, 1968, **3**, 37–46.
69 J. Tauc, R. Grigorovici and A. Vancu, *Phys. Status Solidi*, 1966, **15**, 627–637.
70 E. A. Davis and N. F. Mott, *Philos. Mag. A*, 1970, **22**, 903–922.
71 T. Ansari, A. Pandit, M. Prasad and R. Singh, *Indian J. Phys., A*, 1898, **63**, 784–792.
72 G. Steiner, R. Salzer and W. Reichelt, *Fresenius. J. Anal. Chem.*, 2001, **370**, 731–734.
73 M. Sadeghi, *J. Mater. Sci.: Mater. Electron.*, 2016, **27**, 5796–5801.
74 W. Zhang, J. Yin, F. Min, L. Jia, D. Zhang, Q. Zhang and J. Xie, *J. Mol. Struct.*, 2017, **1127**, 777–783.
75 T. Soga, *Nanostructured materials for solar energy conversion*, Elsevier, Amesterdam, The Netherlands, 2006.
76 M. Radecka, M. Rekas, A. Trenczek-Zajac and K. Zakrzewska, *J. Power Sources*, 2008, **181**, 46–55.
77 F. Fabregat-Santiago, G. Garcia-Belmonte, J. Bisquert, P. Bogdanoff and A. Zaban, *J. Electrochem. Soc.*, 2003, **150**, E293–E298.
78 A. Pitarch, J. Bisquert and G. Garcia-Belmonte, *J. Non-Cryst. Solids*, 2003, **324**, 196–200.
79 M. C. K. Sellers and E. G. Seebauer, *Thin Solid Films*, 2011, **519**, 2103–2110.
80 S. R. Morrison, *Electrochemistry at Semiconductor and Oxidized Metal Electrodes*, Plenum Press, New York, NY, USA, 1980.
81 S. Moghiminia, H. Farsi and H. Raissi, *Electrochim. Acta*, 2014, **132**, 512–523.
82 J. C. Hill, Y. Ping, G. A. Galli and K. Choi, *Energy Environ. Sci.*, 2013, **6**, 2440–2446.
83 N. Joseph, J. Varghese, T. Siponkoski, M. Teirikangas, M. T. Sebastian and H. Jantunen, *ACS Sustainable Chem. Eng.*, 2016, **4**, 5632–5639.
84 W. Wen, C. Li, Y. Sun, Y. Tang and L. Fang, *J. Electron. Mater.*, 2017, **47**, 1003–1008.
85 M. Schalenbach, G. Tjarks, M. Carmo, W. Lueke, M. Mueller and D. Stolten, *J. Electrochem. Soc.*, 2016, **163**, F3197–F3208.
86 H. Zhang, H. Jiang, Y. Hu, Y. Li, Q. Xu, S. Petr and C. Li, *J. Mater. Chem. A*, 2019, **7**, 7548–7552.
87 L. Zhang, J. Xiao, H. Wang and M. Shao, *ACS Catal.*, 2017, **7**, 7855–7865.
88 K. Sardar, E. Petrucco, C. I. Hiley, J. D. Sharman, P. P. Wells, A. E. Russell, R. J. Kashtiban, J. Sloan and R. I. Walton, *Angew. Chem., Int. Ed.*, 2014, **53**, 10960–10964.
89 C. Hu, L. Zhang and J. Gong, *Energy Environ. Sci.*, 2019, **12**, 2620–2645.
90 Y. Gou, L. Yang, Z. Liu, A. M. Asiri, J. Hu and X. Sun, *Inorg. Chem.*, 2018, **57**, 1220–1225.

91 X. Yue, S. Huang, J. Cai, Y. Jin and P. K. Shen, *J. Mater. Chem. A*, 2017, **5**, 7784–7790.
92 J. O. Bockris and T. Otagawa, *J. Phys. Chem.*, 1983, **87**, 2960–2971.
93 L. D. Burke, O. J. Murphy, J. F. O'Neill and S. Venkatesan, *J. Chem. Soc., Faraday Trans. 1*, 1977, **73**, 1659–1671.
94 P. Clechet, C. Martelet, J. R. Martin and R. Olier, *Electrochim. Acta*, 1979, **24**, 457–461.
95 D. A. Denton, J. A. Harrison and R. I. Knowles, *Electrochim. Acta*, 1981, **26**, 1197–1251.
96 B. E. Conway, *Ionic Hydration in Chemistry and Biophysics*, 1981, Elsevier, New York, p. 572.
97 X. Liu, Q. Gao, Y. Zhang, F. Li and Y. Zhang, *Mater. Technol.*, 2016, **31**, 653–657.
98 J. Wang, F. Xu, H. Jin, Y. Chen and Y. Wang, *Adv. Mater.*, 2017, **29**, 1605838.
99 N. Danilovic, R. Subbaraman, D. Strmcnik, K. C. Chang, A. P. Paulikas, V. R. Stamenkovic and N. M. Markovic, *Angew. Chem., Int. Ed. Engl.*, 2012, **51**, 12495.
100 J. Mahmood, F. Li, S. M. Jung, M. S. Okyay, I. Ahmad, S. J. Kim, N. Park, H. Y. Jeong and J. B. Baek, *Nat. Nanotechnol.*, 2017, **12**, 441.
101 W. Sheng, M. Myint, J. G. Chen and Y. Yan, *Energy Environ. Sci.*, 2013, **6**, 1509–1512.
102 W. Sheng, Z. Zhuang, M. Gao, J. Zheng, J. G. Chen and Y. Yan, *Nat. Commun.*, 2015, **6**, 5848.
103 N. M. Markovića, S. T. Sarraf, H. A. Gasteigert and P. N. Ross, *J. Chem. Soc., Faraday Trans.*, 1996, **92**, 3719–3725.
104 N. Danilovic, R. Subbaraman, D. Strmcnik, K. C. Chang, A. P. Paulikas, V. R. Stamenkovic and N. M. Markovic, *Angew. Chem.*, 2012, **124**, 12663–12666.
105 P. F. B. D. Martins, P. P. Lopes, E. A. Ticianelli, V. R. Stamenkovic, N. M. Markovic and D. Strmcnik, *Electrochem. Commun.*, 2019, **100**, 30–33.
106 S. Yamamoto, K. Andersson, H. Bluhm, G. Ketteler, D. E. Starr, T. Schiros, H. Ogasawara, L. G. M. Pettersson, M. Salmeron and A. Nilsson, *J. Phys. Chem. C*, 2007, **111**, 7848–7850.
107 X. Zhang, X. Cui, Y. Sun, K. Qi, Z. Jin, S. Wei, W. Li, L. Zhang and W. Zheng, *ACS Appl. Mater. Interfaces*, 2018, **10**, 745–752.
108 T. F. Jaramillo, K. P. Jørgensen, J. Bonde, J. H. Nielsen, S. Horch and I. Chorkendorff, *Science*, 2007, **317**, 100–102.
109 J. Benson, M. Li, S. Wang, P. Wang and P. Papakonstantinou, *ACS Appl. Mater. Interfaces*, 2015, **7**, 14113–14122.
110 H. Zhong, K. Fujii, Y. Nakano and F. Jin, *J. Phys. Chem. C*, 2015, **119**, 55–61.
111 H. Ooka, M. C. Figueiredo and M. T. M. Koper, *Langmuir*, 2017, **33**, 9307–9313.
112 Y. J. Zhang, V. Sethuraman, R. Michalsky and A. A. Peterson, *ACS Catal.*, 2014, **4**, 3742–3748.
113 M. Le, M. Ren, Z. Zhang, P. T. Sprunger, R. L. Kurtz and J. C. Flake, *J. Electrochem. Soc.*, 2011, **158**, E45–E49.
114 K. Zhao, Y. Liu, X. Quan, S. Chen and H. Yu, *ACS Appl. Mater. Interfaces*, 2017, **9**, 5302–5311.
115 S. Ohya, S. Kaneco, H. Katsumata, T. Suzuki and K. Ohta, *Catal. Today*, 2009, **148**, 329–334.
116 D. Ren, Y. Deng, A. D. Handoko, C. S. Chen, S. Malkhandi and B. S. Yeo, *ACS Catal.*, 2015, **5**, 2714–2821.
117 J. Wu, F. G. Risalvato, S. Ma and X. D. Zhou, *J. Mater. Chem. A*, 2014, **2**, 1647–1651.
118 R. Zhang, W. Lv and L. Lei, *Appl. Surf. Sci.*, 2015, **356**, 24–29.
119 C. W. Lee, N. H. Cho, K. D. Yang and T. Nam, *ChemElectroChem*, 2017, **4**, 2130–2136.
120 E. Tayyebi, J. Hussain, Y. Abghui and E. Skulason, *J. Phys. Chem. C*, 2018, **122**, 10078–10087.